Pulsed Nanogenerator with Huge Instantaneous Output Power Density

Gang Cheng,[†,‡,⊥] Zong-Hong Lin,[†,⊥] Long Lin,[†] Zu-liang Du,[‡] and Zhong Lin Wang[†,§,*]

[†]School of Material Science and Engineering, Georgia Institute of Technology, Atlanta, Georgia 30332-0245, United States, [‡]Key Lab for Special Functional Materials, Henan University, Kaifeng, China, and [§]Beijing Institute of Nanoenergy and Nanosystems, Chinese Academy of Sciences, China. [⊥]G. Cheng and Z.-H. Lin contributed equally to this work.

ABSTRACT A nanogenerator (NG) usually gives a high output voltage but low output current, so that the output power is low. In this paper, we developed a general approach that gives a hugely improved instantaneous output power of the NG, while the entire output energy stays the same. Our design is based on an off—on—off contact based switching during mechanical triggering that largely reduces the duration of the charging/discharge process, so that the instantaneous output current pulse is hugely improved without sacrificing the output voltage. For a vertical contact-separation mode triboelectric NG (TENG), the instantaneous output current and power peak can reach as high as 0.53 A and 142 W at a load of 500 Ω, respectively. The corresponding instantaneous output current and power density peak even approach 1325 A/m^2 and 3.6 × 10^5 W/m^2, which are more than 2500 and 1100 times higher than the previous records of TENG, respectively. For the rotation disk based TENG in the lateral sliding mode, the instantaneous output current and power density of 104 A/m^2 and 1.4 × 10^4 W/m^2 have been demonstrated at a frequency of 106.7 Hz. The approach presented here applies to both a piezoelectric NG and a triboelectric NG, and it is a major advance toward practical applications of a NG as a high pulsed power source.
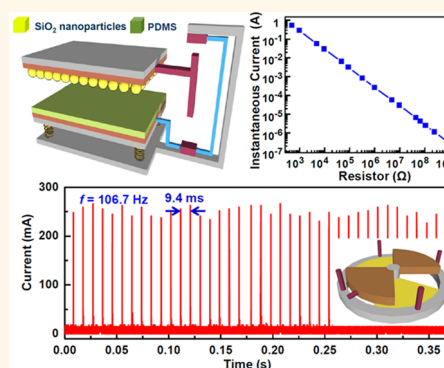
KEYWORDS: triboelectric nanogenerator · instantaneous discharging

Harvesting mechanical energy from the ambient environment and the human body has attracted increasing interest for large-scale energy needs and nanoscale self-powered electronic devices.[1−4] Approaches based on utilizing various physical mechanisms, such as electromagnetic,[5,6] electrostatic,[7,8] and piezoelectric[9−13] effects, have been realized to harvest mechanical energy. Recently, a triboelectric nanogenerator (TENG)[14−23] based on contact electrification effects[24−26] has been invented as a new energy technology for efficiently converting mechanical vibrations into electricity. Various applications of TENG have been demonstrated, such as self-powered chemical sensors,[27,28] electrodegradation,[29] and powering commercial LEDs.[19] With the periodic contact and separation of two triboelectric surfaces (tribo-surfaces) with opposite triboelectric charges (tribo-charges), the potential difference between metal electrodes of the two tribo-surfaces periodically varies, which drives the inductive charging/discharging between the two electrodes. For the traditional TENG, the two electrodes are directly connected by metal wires; therefore, the inductive charges are continuously charged/discharged during the entire contact-separation process between the two tribo-surfaces. This configuration of TENG is defined here as the continuous discharging (CD) TENG. Since the total triboelectric-induced charges are constant, the output current of the CD-TENG depends on the working frequency.[17] Placing springs between two tribo-surfaces[19] and designing a rotating disk TENG[23] are demonstrated as effective methods to increase the contact-separation speed and enhance the output current. However, up to now, the record of output current density of the CD-TENG is only 0.52 A/m^2,[19] and the output voltage and power decrease sharply as the external load is lower than 1 MΩ.[19,23] Given that the working frequency of the TENG cannot unlimitedly increase, it is important to explore novel methods to enhance the electric output of a TENG for largely expanding its applications.

In this paper, we developed an instantaneous discharging (ID) TENG by introducing

a "switch" in the electrode contact, which can gigantically enhance the instantaneous output power. The electrodes of ID-TENG are connected through an electric switch triggered by the moving of the TENG, and the inductive charges are charged/discharged instantaneously as the triggered switch is closed. As for both the contact-separation mode and the sliding rotation mode, the instantaneous output power of the TENG has been improved by several orders of magnitude, which largely expands the applications of TENGs.

RESULTS AND DISCUSSION

The fabrication processes of the ID-TENG with vertical contact-separation mode are shown in Figure 1a. Poly(methyl methacrylate) (PMMA) plates are chosen to construct the device due to its low cost, light weight, decent strength, and easy processing. First, thin layers of Au thin film are deposited on two PMMA plates as the metal electrodes. The Au electrodes in the upper and lower plates are called the top electrode and back electrode for later reference, respectively. On the lower plate, a layer of polydimethylsiloxane (PDMS) is further coated on the back electrode as the contact material. The elastic property of PDMS enables a complete contact of two tribo-surfaces despite the surface roughness. On the upper plate, a layer of SiO_2 nanoparticles (NPs) is assembled on the top electrode as the other contact material. SiO_2 NPs were synthesized according to the Stöber method.[30,31] Then an Al needle (K_0) is connected to the top electrode as one side of the triggered switch. Two Al sheets (K_1 and K_2) are attached to the back electrode as the other side of the triggered switch, which are positioned above the upper plate and

below the lower plate, respectively. Finally, the lower plate is placed on a PMMA base through four springs. The springs were used for the purpose of ensuring the triggered switch is opened when the two tribo-surfaces are contacted. Figure 1b shows the SEM image of the SiO_2 NP layers assembled on the deposited Au film. The SiO_2 NPs have an average diameter of 240 nm and are uniformly dispersed on the Au film. Using NPs can increase the effective contact area of materials and enhance the electric output of the TENG.[19]

The electricity generation mechanism of the ID-TENG is sketched in Figure 2. At the initial state (Figure 2a), there are no tribo-charges on the two tribo-surfaces. When a force is applied, the upper plate moves downward, and the tribo-charges are generated when the two tribo-surfaces are contacted with each other. According to the triboelectric series that ranks materials' tendency to gain or lose electrons, electrons are injected from SiO_2 into PDMS,[24] resulting in positive and negative tribo-charges on the SiO_2 and PDMS surface, respectively (Figure 2b). With the further downward movement of the top plate, the springs are compressed, and the lower plate moves downward together with the upper plate and finally touches the PMMA base. The length of K_0 is accurately adjusted to ensure that K_0 can contact K_2 only when the lower plate touches the PMMA base. At the state of Figure 2b, although the triggered switch is closed, the potential difference between the two electrodes is vanishingly small, so that there is little force to drive the inductive charges, if any, to flow. As the force is withdrawn and the upper plate moves upward, due to the restoring force of the compressed springs, K_0 is detached from K_2
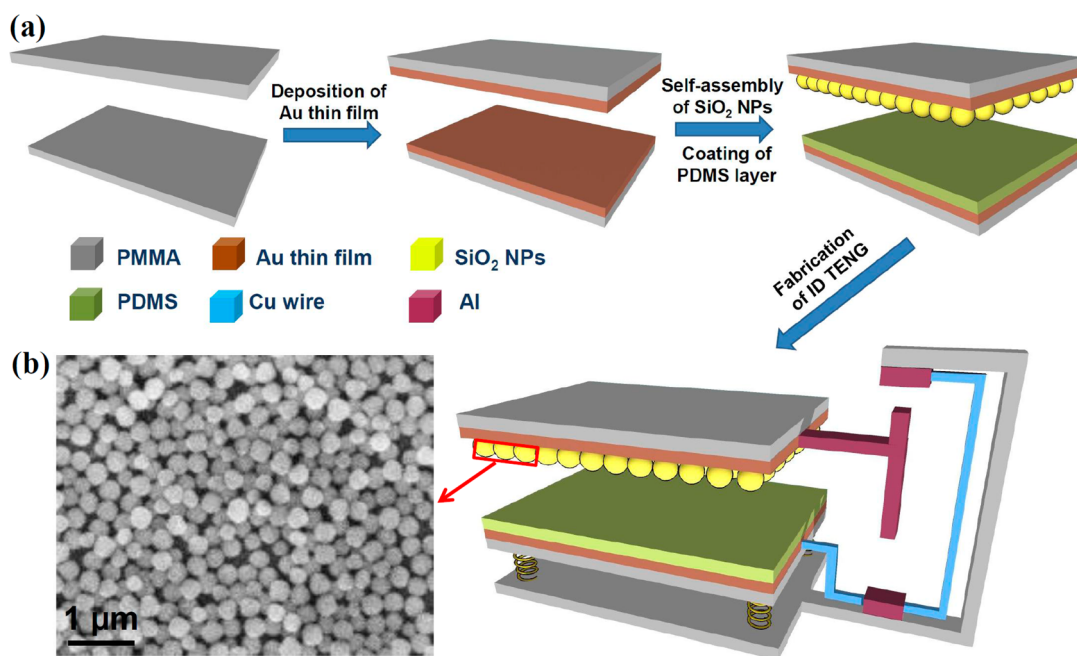

(a)

Deposition of Au thin film

Self-assembly of SiO_2 NPs

Coating of PDMS layer

Fabrication of ID TENG

PMMA Au thin film SiO_2 NPs
PDMS Cu wire Al

(b)

1 μm

Figure 1. (a) Diagram of the fabrication processes of the instantaneous discharging TENG. (b) SEM image of SiO_2 NPs assembled on a Au film, which enhances the triboelectrification.
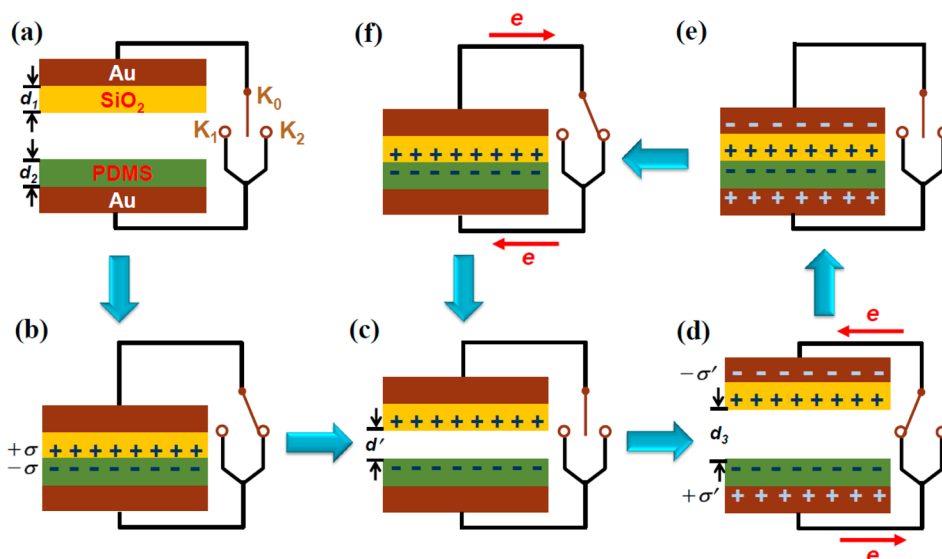
Figure 2. Working mechanism of the ID-TENG. (a) Initial state without tribo-charges. (b) Contact between two tribo-surfaces generates tribo-charges. (c) The triggered switch is opened as the two tribo-surfaces are separated, and no inductive charges are generated in the electrodes. (d) At the moment when the triggered switch is closed, the inductive charges are instantaneously charged to the electrodes. (e) When the two tribo-surfaces contact each other, the triggered switch is still opened, and the inductive charges still remain on the electrodes. (f) At the moment when the triggered switch is closed, the inductive charges are instantaneously discharged.

first, and then the two tribo-surfaces are separated. As a result, in the separation process of the two plates, the triggered switch is opened, and the inductive charges cannot flow between the two electrodes (Figure 2c). In this process, the potential difference between the two electrodes is generated. Here, we define the potential of the back electrode as zero and the potential of the top electrode as V_{ID}. In the process of Figure 2c, V_{ID} is positive and increases with d' (the distance between the two tribo-surfaces). When d' increases to d_3, K_0 will contact K_1 to make the triggered switch close, and then the inductive charges are intanstaneously allowed to flow between the two electrodes to screen V_{ID} (Figure 2d). Before the instantaneous charging process, V_{ID} reaches its positive maximum value (V_{ID-M}^+), which can be expressed by[16]

$$V_{ID-M}^+ = \frac{\sigma S}{C_3} \qquad (1)$$

where σ is the tribo-charge density, S is the contact area between the two tribo-surfaces, and C_3 is the capacitance composed by the air layer between the two tribo-surface with a thickness of d_3. The generated positive current (I_{ID}^+) in this process can be expressed by

$$I_{ID}^+ = \frac{V_{ID-M}^+}{R} e^{-t/\tau_+} \qquad (2)$$

where R is the resistance of the external load in the circuit, τ_+ is time decay constant for I_{ID}^+ and is equal to RC_{123}, C_{123} is the capacitance composed by the serially connected three dielectric layers of the SiO$_2$ layer with thickness d_1, the air layer with thickness d_3, and PDMS layer with thickness d_2. At $t = 0$ (the moment as

the triggered switch is closed), I_{ID}^+ reaches its maximum value I_{ID-M}^+ and then decays exponentially with time.

Discussed above is the first half-cycle of the ID-TENG. As a start of another half-cycle, the upper plate begins to move downward, K_0 is detached from K_1, and the triggered switch is opened. As the two tribo-surfaces have contacted each other and the springs have not been compressed, K_0 cannot contact K_2 and the triggered switch is still opened. Therefore, the inductive charges still remain on the two electrodes (Figure 2e). At this state, the positive potential caused by tribo-charges decreases to zero, V_{ID} is dominated by the negative potential caused by inductive charges and reaches its maximum absolute value (I_{ID-M}^-), which is expressed by

$$V_{ID-M}^- = \frac{\sigma' S}{C_{12}} \qquad (3)$$

where σ' is the density of inductive charges in the state of Figure 2e and C_{12} is the capacitance composed by the two serially connected dielectric layers of SiO$_2$ and PDMS. In order to increase I_{ID-M}^- and the corresponding negative electric output, a PDMS layer with a thickness of 1 mm is used to decrease C_{12} in our experiment. With the further downward movement of the upper plate, the springs are compressed, and then K_0 contacts K_2 to make the triggered switch close. Consequently, the inductive charges are instantaneously allowed to flow between the two electrodes, and σ' and V_{ID} become zero under electric equilibrium (Figure 2f). The generated negative current (I_{ID}^-) in this process can be expressed by

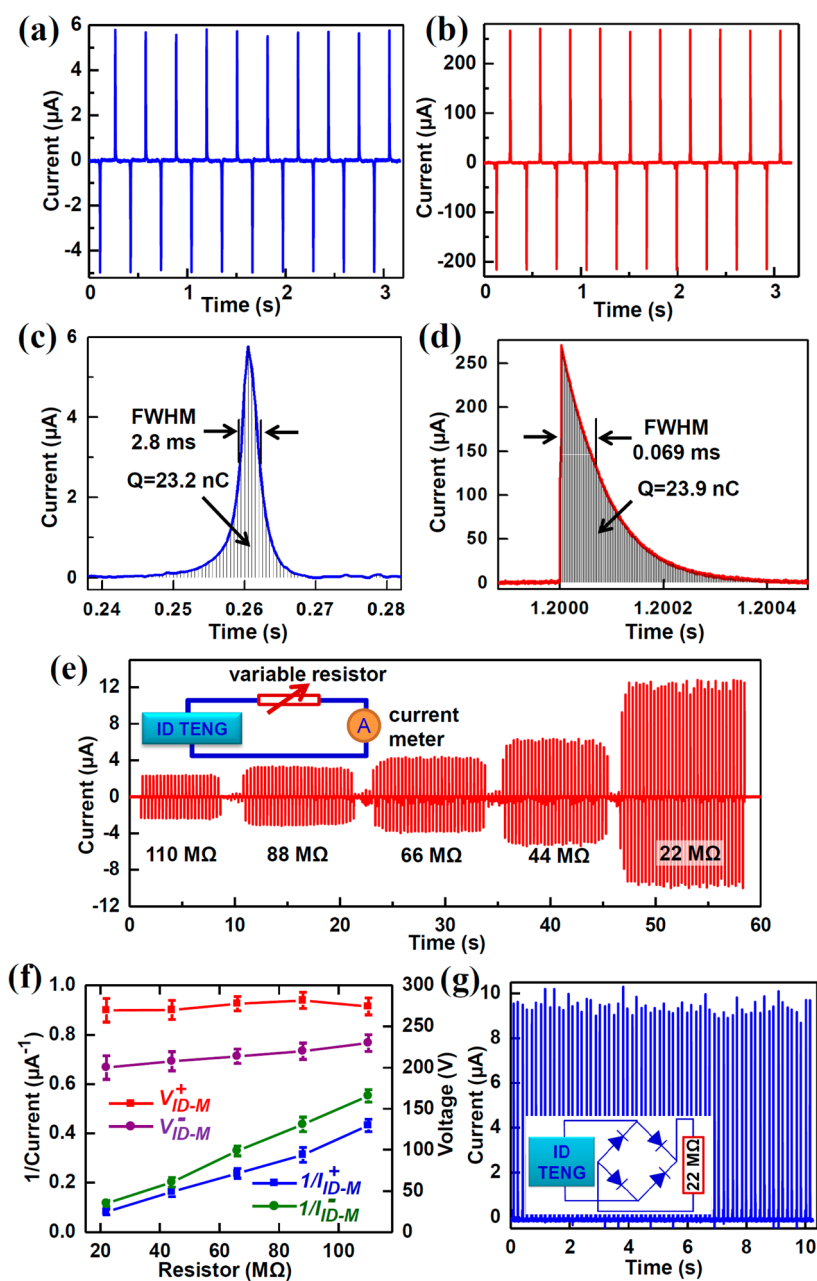$$I_{ID}^- = -\frac{V_{ID-M}^-}{R} e^{-t/\tau_-} \qquad (4)$$

Figure 3. Output current characterisitcs of the CD-TENG without load (a) and the ID-TENG with a load of 1 MΩ (b). Magnification of a single current peak of the CD-TENG (c) and the ID-TENG (d). (e) Current of the ID-TENG at variable load ranging from 110 to 22 MΩ. (f) Dependence of $V_{ID}^{\pm}{}_{-M}$ and $1/I_{ID}^{\pm}{}_{-M}$ on load resistance. (g) Current of the ID-TENG at a load of 22 MΩ by using a full-wave rectifying bridge, and the inset shows the measurement diagram.

where τ_- is the time decay constant for I_{ID}^- and is equal to RC_{12}. At $t = 0$, I_{ID}^- reaches its maximum absolute value I_{ID-M}^- and then decays exponentially with time. The expressions of C_1, C_{12}, C_{123}, σ', and the equation deduction of current are shown in the Supporting Information. When the upper plate moves upward again, a new cycle starts (Figure 2c to f).

At first, the output performances of the same TENG device with ID and CD configurations were compared. For measuring the CD-TENG, a Cu wire was used to directly connect the top electrode and back electrode. The TENG devices were mechanically triggered by a

linear motor that provided dynamic impact with a controlled force at a frequency of 3.3 Hz. Due to the limitation of the range and bandwidth of our current meter (5 mA, 1 MHz), an external load of more than 1 MΩ needs to be serially connected to the circuit of the ID-TENG. The electric output of the ID-TENG with lower external load will be discussed later by using an oscilloscope. The short-circuit current of the CD-TENG without an external load and the current of the ID-TENG with a load of 1 MΩ measured by a current meter are shown in Figure 3a and b, respectively. Even when a load of 1 MΩ is connected to the ID-TENG,

the current peak of the ID-TENG (about 264 μA) is 45 times higher than that of the CD-TENG (about 5.7 μA), which demonstrates the pronounced enhancement of current. The magnifications of a single current peak of the CD- and ID-TENG are shown in Figure 3c and d, respectively. For the CD-TENG, the current increases slowly from zero to the peak and then decreases slowly from the peak to zero, and the two processes are almost symmetric. The full-width of half-maximum (fwhm) of the peak is 2.8 ms, and the integral area of the peak is 23.2 nC. For the ID-TENG, the current increases abruptly from zero to its peak and then decreases slowly from peak to zero. The fwhm of the peak is 0.069 ms, and the integral area of the peak is 23.9 nC. From the above comparisons, it is clear that the CD- and ID-TENG have nearly equal amounts of inductive charges, while the ID-TENG has a much faster charging/discharging speed than the CD-TENG. For the CD-TENG, this speed is limited by the mechanical contact-separation speed between the two tribo-surfaces. For the ID-TENG, this speed is not limited by the mechanical contact-separation speed, and the inductive charges can be instantaneously charged/discharged as the triggered switch is closed, which is the essential reason for the enhancement of the current. The open-circuit voltages (V_{OC}) of the CD-TENG and the ID-TENG are both about 285 V (Supplementary Figure S1), which is attributed to the ID-TENG having an equivalent circuit configuration to the CD-TENG in the open-circuit condition.

Figure 3e shows the current of the ID-TENG with variable external load from 110 to 22 MΩ, which indicates that the current peak increases with the decrease of resistance. According to eqs 2 and 4, the positive and negative current peaks ($I_{ID-M}^{\pm}$) are equal to $V_{ID-M}^{\pm}/R$ and inversely proportional to R. In order to verify this relationship, the mean values of the current peaks at each resistance are calculated using the data in Figure 3e, and the plots of $1/I_{ID-M}^{\pm}$ vs R are shown in Figure 3f, which are nearly linear and accord well with the equations. As shown in Figure 3e, I_{ID-M}^{+} is slightly higher than I_{ID-M}^{-}, which means that V_{ID-M}^{+} is slightly higher than V_{ID-M}^{-}. By calculating the peaks for more than 400 cycles at a load of 22 MΩ (Supplementary Figure S2), it is obtained that the mean values of V_{ID-M}^{+} and V_{ID-M}^{-} and their ratio are 269 V, 206 V, and 1.3, respectively. According to eqs 1 and 3 and the relative expression in the Supporting Information, the lower value of V_{ID-M}^{-} is attributed to the thickness of the PDMS layer (d_2, about 1 mm) being lower than the separated distance between the two tribo-surfaces (d_3, about 4 mm in our experiment). Equations 1 and 3 also indicate that $V_{ID-M}^{\pm}$ do not vary with R. In order to verify this point, the mean values of $V_{ID-M}^{\pm}$ at each resistance are calculated using the data in Figure 3e and are plotted in Figure 3f, which confirms that $V_{ID-M}^{\pm}$ stays nearly constant for variable R. In addition,

the ac output of the ID-TENG could be transferred to pulse output in the same direction simply by using a full-wave rectifying bridge, as shown in Figure 3g.

The electric output performances of the ID-TENG with an external load from 500 Ω to 1 GΩ were measured by oscilloscope (see Supplementary Figure S3 for the diagram of measurement circuit). The positive and negative electric outputs have similar performances and tendency, so the positive electric outputs are discussed in detail here, and the negative outputs are shown in Supplementary Figure S4. Figure 4a shows the current peak of the ID-TENG with an external load of 1 KΩ, in which an ultrahigh instantaneously maximum current of 290 mA is obtained. In the plot of this curve in semilog scale (inset of Figure 4a), the logarithm of the current decreases linearly with time and can be fitted by a straight line. According to eq 2, the corresponding time decay constant τ is obtained as 0.24 μs by calculating the slope of the fitted line. By fitting the current peaks of the ID-TENG at variable resistances, the τ values for variable resistances are obtained and plotted in Figure 4b in log scale. In the range from 500 Ω to 1 GΩ, τ increases linearly with R and can be fitted by a straight line. By calculating the slope of the fitted line according to the expression $\tau = RC_{123}$, C_{123} is calculated as 129 pF.

For comparing the performances between the ID- and CD-TENG, the current and voltage of the CD-TENG with an external load from 500 Ω to 1 GΩ were measured by current and voltage meters, and the dependences of its instantaneously maximum voltage, current, and power (V_{CD-M}, I_{CD-M}, and W_{CD-M}) on load are shown in Supplementary Figure S5. The average value and the statistical error of V_{ID-M} are calculated from 10 curves at each load, and the dependences of V_{ID-M} and V_{CD-M} on load are compared in Figure 4c. V_{ID-M} nearly keeps constant around 280 V in the resistance range from 500 Ω to 1 GΩ, which shows that V_{ID-M} is independent of R and accords well with eq 1. V_{CD-M} decreases gradually as R decreases from 1 GΩ to 1 MΩ and nearly drops to zero when R is less than 1 MΩ. The dependences of I_{ID-M} and I_{CD-M} on load are compared in Figure 4d. For the CD-TENG, as R decreases from 1 GΩ to 10 MΩ, I_{CD-M} gradually increases, while I_{CD-M} does not increase further when R is less than 10 MΩ and its maximum value is about 6 μA. For the ID-TENG, I_{ID-M} increases with the decrease in resistance in the range from 1 GΩ to 500 Ω and reaches its instantaneously maximum value of 0.53 A at 500 Ω. The maximum value of I_{ID-M} is about 5 orders of magnitude higher than that of I_{CD-M}, which indicates a gigantic enhancement of the output current. The corresponding instantaneously maximum current density is 1325 A/m^2, which is 2548 times higher than the previous record of TENG.[19] The plot of I_{ID-M} with R is nearly a straight line with a slope of -1 in the log scale (Figure 4d), and this means that
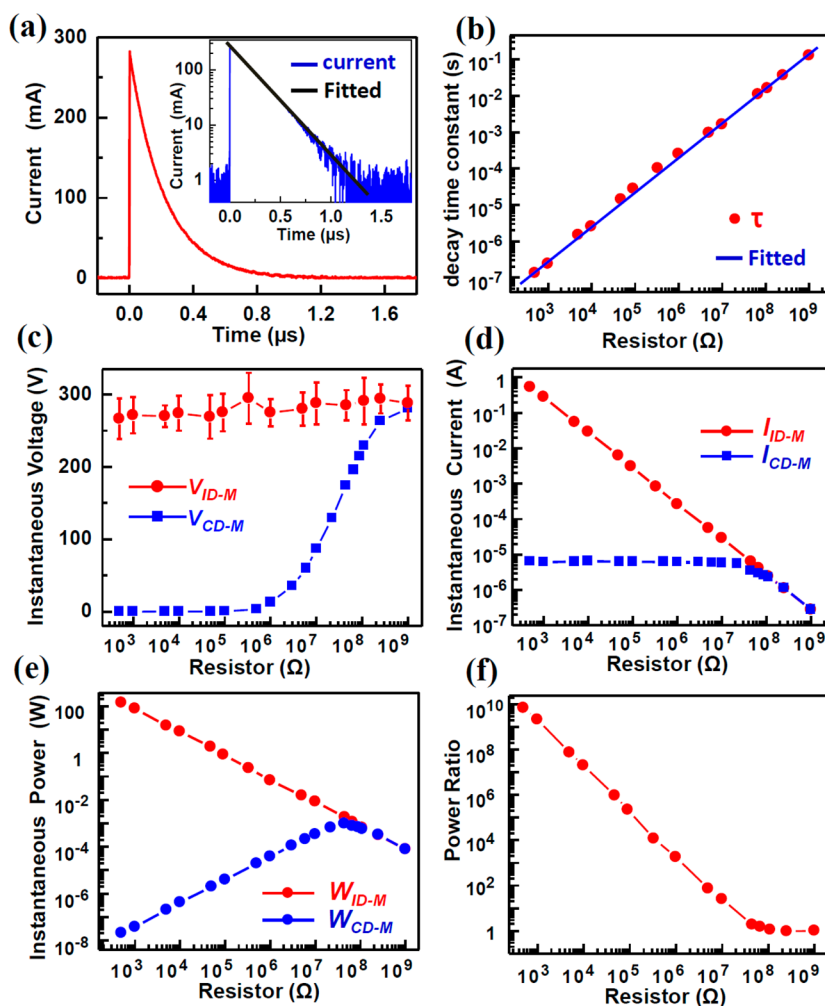
Figure 4. (a) Current of the ID-TENG at a load of 1 KΩ; inset shows the curve in semilog scale and its fitted line. (b) Dependence of τ on resistance and its fitted line. (c) Dependence of V_{ID-M} and V_{CD-M} on resistance. (d) Dependence of I_{ID-M} and I_{CD-M} on resistance. (e) Dependence of W_{ID-M} and W_{CD-M} on resistance. (f) Dependence of the power ratio (W_{ID-M}/W_{CD-M}) on resistance.

$I_{ID-M} \propto R^{-1}$ and accords well with the current expression in eq 2. The instantaneously maximum output power of ID-TENG (W_{ID-M}) on an external load is calculated as $W_{ID-M} = I_{ID-M}^2 R$, and the dependences of W_{ID-M} and W_{CD-M} on R are plotted in Figure 4e. For the CD-TENG, W_{CD-M} reaches its peak of 0.97 mW as R decreases to 44 MΩ, then decreases with decreasing R, and W_{CD-M} at 500 Ω decreases to 18.8 nW. For the ID-TENG, W_{ID-M} increases with decreasing R in the range from 1 GΩ to 500 Ω and reaches the instantaneously maximum power of 142 W at 500 Ω. The maximum value of W_{ID-M} (at 500 Ω) is more than 5 orders of magnitude higher than that of W_{CD-M} (at 44 MΩ). The corresponding instantaneously maximum power density of ID-TENG at 500 Ω is 3.6×10^5 W/m^2, which is 1150 times higher than the previous record of TENG.[19] The plot of W_{ID-M} with R is nearly a straight line with a slope of -1 in the log scale (Figure 4d), which means $W_{ID-M} \propto R^{-1}$. The ratio values of W_{ID-M}/W_{CD-M} at each load are calculated, and the dependence of the ratio values on resistance is shown in Figure 4f.

For a load resistance of more than 100 MΩ, the ratio is nearly equal to 1. When the load resistance is less than 100 MΩ, the ratio value increases with decreasing resistance, and the ratio is about 10^{10} at 500 Ω, which indicates a gigantic enhancement in instantaneous power, especially at low load resistance.

Up to now, TENGs with various working modes have been developed, such as vertical contact-separation,[19] in-plane sliding,[21,22] and rotation disk.[23] The ID-TENG device discussed above is based on a vertical contact-separation mode. The ID-TENG configuration is essentially suitable for all TENG modes; therefore, the ID-TENG devices with in-plane sliding and rotation disk modes have also been fabricated. The structure diagram and electric output performances of the in-plane sliding ID-TENG are shown in Supplementary Figure S6, in which the instantaneous current and power can reach 57.5 mA and 3.3 W, respectively. Due to the high working frequency of TENG with rotation disk mode,[23] the ultrahigh electric output with high working frequency is expected if combining the ID-TENG
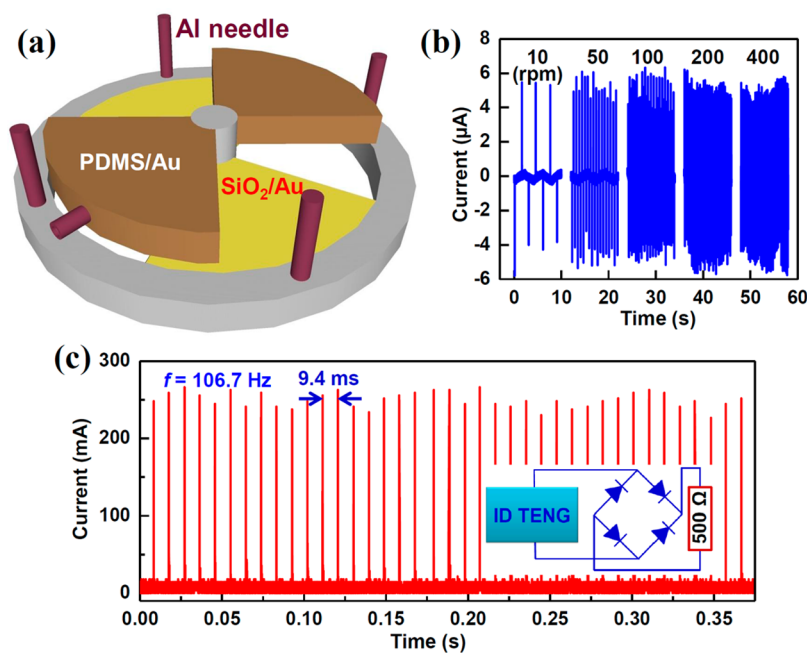
Figure 5. (a) Diagram of ID-TENG with rotation disk mode. (b) Current of rotation disk ID-TENG at variable speed from 10 to 400 rpm. (c) Current of rotation disk ID-TENG at a speed of 1600 rpm and a load of 500 Ω by using a full-wave rectifying bridge, and inset shows the measurement diagram.

configuration with the rotation disk mode. Figure 5a shows the diagram of the rotation disk ID-TENG. The basic structure is composed of two disk-shaped components with two sectors each, and the tribo-surfaces and electrodes use same materials and structures as the vertical contact-separation ID-TENG shown in Figure 1. The Au electrodes of the two sectors in the top disk are connected together, and an Al needle is attached to the electrode of one sector to act as one side of the triggered switch; four Al needles are connected to the back electrode to act as the other side of the triggered switch. When the two tribo-surfaces are fully contacted or separated, the Al needle connected to the top electrode will make contact with one of the Al needles connected to the back electrode to close the triggered switch, and then the inductive charges are instantaneously allowed to flow between the two electrodes. The V_{OC} of the rotation disk ID-TENG is about 115 V (Supplementary Figure S7), and the current with a load of 22 MΩ at variable rotation speed was measured by a current meter and is shown in Figure 5b. In the range from 10 to 400 rounds per minute (rpm), the current peaks stay constant around 5.2 μA, which verifies that the contact-separation speed between two tribo-surfaces does not influence the current of the ID-TENG. The electric output performances at a lower load were measured by an oscilloscope, and the current at a rotation speed of 1600 rpm and a load of 500 Ω by using a full-wave rectifying bridge is shown in Figure 5c. The instantaneously maximum current and power peaks are 0.26 A and 33.8 W, and the corresponding instantaneous current and power density peaks are 104 A/m² and

1.4 × 10⁴ W/m², respectively. The interval between two peaks is 9.4 ms, and the corresponding working frequency is 106.7 Hz. This result shows the capability of the rotation disk ID-TENG to provide ultrahigh electric outputs with high frequency. In addition, a piezoelectric nanogenerator (NG) is another widely investigated NG to harvest mechanical energy, which is based on the piezoelectric effect.[9−13] It has been reported that the piezoelectric NG can reach an output voltage of more than 200 V and power light-emitting diode.[32,33] Due to the similar working modes between a piezoelectric NG and a triboelectric NG, it is expected that the instantaneous discharging mode can also be applied to a piezoelectric NG to improve the instantaneous output power and widen the applications of the piezoelectric NG.

CONCLUSION

In summary, we have developed an approach that can gigantically enhance the instantaneous electric outputs of the TENG. The electrodes of ID-TENG are connected through an electric switch triggered by moving the TENG, and the inductive charges are instantaneously charged/discharged as the triggered switch is closed. In the vertical contact-separation mode, the instantaneously maximum current peak of the ID-TENG of 0.53 A is about 5 orders of magnitude higher than that of the CD-TENG, and the instantaneously maximum current density peak of 1325 A/m² is more than 2500 times higher than the previous record. The instantaneously maximum power peak of ID-TENG of 142 W is more than 5 orders of magnitude higher than that of CD-TENG, and the instantaneously

maximum power density peak of 3.6×10^5 W/m^2 is more than 1100 times higher than the previous record of TENG. By combining the ID-TENG configuration and rotation disk mode, the ultrahigh electric output density peaks of 104 A/m^2 and 1.4×10^4 W/m^2 are demonstrated at a high frequency of 106.7 Hz.

The gigantic enhancement of instantaneous output power overcomes the bottleneck for the applications of TENG in some cases. Lastly, we must point out that, although the instantaneous power peak is enhanced, the total output energy remains about the same for both ID-TENG and DC-TENG.

METHODS SUMMARY

Synthesis and Self-Assembly of SiO$_2$ NPs. SiO$_2$ NPs were synthesized according to the Stöber method.[30] Typically, concentrated ammonia (28%, 3 mL) was added rapidly to the solution containing absolute ethanol (99.9%, 50 mL) and tetraethyl orthosilicate (99%, 1.5 mL). The mixture was reacted at ambient temperature for 24 h. The size of the SiO$_2$ NPs was verified by SEM; they appeared to be nearly monodispersed, with an average size of 240 nm. The functionalization of SiO$_2$ NPs was carried out by mixing the silica NPs with 3-mercaptopropyltrimethoxysilane (95%, 25 μL) for 2 h to promote covalent bonding of the organosilane to the surface of the silica NPs.[31] The solution was then subjected to cycles of centrifugation/wash; centrifugation was conducted at 6000 rpm for 20 min, and absolute ethanol (50 $\times$ 3 mL) was used to wash the pellets. Finally, the sputtered Au thin film was dipped into the solution of functionalized SiO$_2$ NPs for 12 h to allow complete assembly of a few layers of SiO$_2$ NPs.

Fabrication of the ID-TENG. First, two PMMA sheets (thickness of 0.3 cm) were processed by laser cutting (PLS6.75, Universal Laser Systems) to form two plates with square or disk shapes. Au films of 100 nm were deposited on both of the PMMA plates by an e-beam evaporator. On one of the plate, fluid PDMS that consists of base and curing agent in a ratio of 10:1 was spin-coated multiple times to form a 1 mm thick layer. Then it was cured at 60 °C for 12 h. On the other plate, SiO$_2$ NPs were assembled on the deposited Au film. For a vertical contact-separation ID-TENG, an Al needle and two Al sheets were connected to the gold films of the top plate and bottom plate to act as a triggered switch. Then springs were used to construct the complete ID-TENG. The contact area of the device is 4 cm^2. For the rotation disk ID-TENG, the Al needles were connected to the Au films of the top disk and bottom disk to act as a triggered switch. The contact area of the two disks is 25 cm^2.

Electric Output Measurement of ID-TENG. In the electric output measurement, one plate was bonded onto a linear motor for vertical contact-separation mode or onto a spinning motor for rotation disk mode, and the other plate was bonded onto a stationary XYZ linear translation stage. The current meter (SR570 low-noise current amplifier, Stanford Research System) and voltage meter (6514 system electrometer, Keithley) were used to measure the electric outputs of CD-TENG and ID-TENG with an external load of more than 1 MΩ. An oscilloscope (TDS3014B, Tektronix) was used to measure the output voltage and current of ID-TENG with an external load from 500 Ω to 1 GΩ.

Conflict of Interest: The authors declare no competing financial interest.

Supporting Information Available: More detailed information about equation deduction, open-circuit voltage curves of the CD-TENG and the ID-TENG, the current curve with multiple cycles of ID-TENG at a load of 22 MΩ, the measurement diagram of the ID-TENG using an oscilloscope, the negative electric output performance of the ID-TENG, the dependence of output performances on external load of the CD-TENG, the structure diagram and electric output performance of the ID-TENG with in-plane sliding mode, and the open-circuit voltage curve of the ID-TENG with rotation disk mode. This material is available free of charge *via* the Internet at http://pubs.acs.org.

REFERENCES AND NOTES

1. Beeby, S. P.; Tudor, M. J.; White, N. M. Energy Harvesting Vibration Sources for Microsystems Applications. *Meas. Sci. Technol.* **2006**, *17*, R175–R195.

2. Mitcheson, P. D.; Yeatman, E. M.; Rao, G. K.; Holmes, A. S.; Green, T. C. Energy Harvesting from Human and Machine Motion for Wireless Electronic Devices. *Proc. IEEE* **2008**, *96*, 1457–1486.

3. Wang, Z. L.; Wu, W. Z. Nanotechnology-Enabled Energy Harvesting for Self-Powered Micro-/Nanosystems. *Angew. Chem., Int. Ed.* **2012**, *51*, 11700–11721.

4. Wang, Z. L.; Zhu, G.; Yang, Y.; Wang, S. H.; Pan, C. F. Progress in Nanogenerators for Portable Electronics. *Mater. Today* **2012**, *15*, 532–543.

5. Williams, C. B.; Shearwood, C.; Harradine, M. A.; Mellor, P. H.; Birch, T. S.; Yates, R. B. Development of an Electromagnetic Micro-generator. *Proc. IEEE Circ. Dev. Syst.* **2001**, *148*, 337–342.

6. Beeby, S. P.; Torah, R. N.; Tudor, M. J.; Glynne-Jones, P.; O'Donnell, T.; Saha, C. R.; Roy, S. A Micro Electromagnetic Generator for Vibration Energy Harvesting. *J. Micromech. Microeng.* **2007**, *17*, 1257–1265.

7. Mitcheson, P. D.; Miao, P.; Stark, B. H.; Yeatman, E. M.; Holmes, A. S.; Green, T. C. MEMS Electrostatic Micropower Generator for Low Frequency Operation. *Sens. Actuators A* **2004**, *115*, 523–529.

8. Naruse, Y.; Matsubara, N.; Mabuchi, K.; Izumi, M.; Suzuki, S. Electrostatic Micro Power Generation from Low-Frequency Vibration Such As Human Motion. *J. Micromech. Microeng.* **2009**, *19*, 094002.

9. Wang, Z. L.; Song, J. H. Piezoelectric Nanogenerators Based on Zinc Oxide Nanowire Arrays. *Science* **2006**, *312*, 242–246.

10. Qin, Y.; Wang, X. D.; Wang, Z. L. Microfiber-Nanowire Hybrid Structure for Energy Scavenging. *Nature* **2008**, *451*, 809–813.

11. Chang, C. E.; Tran, V. H.; Wang, J. B.; Fuh, Y. K.; Lin, L. W. Direct-Write Piezoelectric Polymeric Nanogenerator with High Energy Conversion Efficiency. *Nano Lett.* **2010**, *10*, 726–731.

12. Chen, X.; Xu, S. Y.; Yao, N.; Shi, Y. 1.6 V Nanogenerator for Mechanical Energy Harvesting Using PZT Nanofibers. *Nano Lett.* **2010**, *10*, 2133–2137.

13. Hu, Y. F.; Lin, L.; Zhang, Y.; Wang, Z. L. Replacing a Battery by a Nanogenerator with 20 V Output. *Adv. Mater.* **2012**, *24*, 110–114.

14. Fan, F. R.; Tian, Z. Q.; Wang, Z. L. Flexible Triboelectric Generator. *Nano Energy* **2012**, *1*, 328–334.

15. Fan, F. R.; Lin, L.; Zhu, G.; Wu, W. Z.; Zhang, R.; Wang, Z. L. Transparent Triboelectric Nanogenerators and Self-Powered Pressure Sensors Based on Micropatterned Plastic Films. *Nano Lett.* **2012**, *12*, 3109–3114.

16. Zhu, G.; Pan, C. F.; Guo, W. X.; Chen, C. Y.; Zhou, Y. S.; Yu, R. M.; Wang, Z. L. Triboelectric-Generator-Driven Pulse Electrodeposition for Micropatterning. *Nano Lett.* **2012**, *12*, 4960–4965.

17. Wang, S. H.; Lin, L.; Wang, Z. L. Nanoscale Triboelectric-Effect-Enabled Energy Conversion for Sustainably Powering Portable Electronics. *Nano Lett.* **2012**, *12*, 6339–6346.

18. Zhang, X. S.; Han, M. D.; Wang, R. X.; Zhu, F. Y.; Li, Z. H.; Wang, W.; Zhang, H. X. Frequency-Multiplication High-Output Triboelectric Nanogenerator for Sustainably Powering Biomedical Microsystems. *Nano Lett.* **2013**, *13*, 1168–1172.

19. Zhu, G.; Lin, Z.-H.; Jing, Q. S.; Bai, P.; Pan, C. F.; Yang, Y.; Zhou, Y. S.; Wang, Z. L. Toward Large-Scale Energy Harvesting by a Nanoparticle-Enhanced Triboelectric Nanogenerator. *Nano Lett.* **2013**, *13*, 847–853.

20. Yang, Y.; Lin, L.; Zhang, Y.; Jing, Q. S.; Hou, T. C.; Wang, Z. L. Self-Powered Magnetic Sensor Based on a Triboelectric Nanogenerator. *ACS Nano* **2012**, *6*, 10378–10383.

21. Wang, S. H.; Lin, L.; Xie, Y. N.; Jing, Q. S.; Niu, S. M.; Wang, Z. L. Sliding-Triboelectric Nanogenerators Based on In-Plane Charge-Separation Mechanism. *Nano Lett.* **2013**, *13*, 2220–2225.

22. Zhu, G.; Chen, J.; Liu, Y.; Bai, P.; Zhou, Y. S.; Jing, Q. S.; Pan, C. F.; Wang, Z. L. Linear-Grating Triboelectric Generator Based on Sliding Electrification. *Nano Lett.* **2013**, *13*, 2282–2289.

23. Lin, L.; Wang, S. H.; Xie, Y. N.; Jing, Q. S.; Niu, S. M.; Hu, Y. F.; Wang, Z. L. Segmentally Structured Disk Triboelectric Nanogenerator for Harvesting Rotational Mechanical Energy. *Nano Lett.* **2013**, *13*, 2916–2923.

24. Castle, G. S. P. Contact Charging between Insulators. *J. Electrostat.* **1997**, *40−41*, 13–20.

25. McCarty, L. S.; Whitesides, G. M. Electrostatic Charging Due to Separation of Ions at Interfaces: Contact Electrification of Ionic Electrets. *Angew. Chem., Int. Ed.* **2008**, *47*, 2188–2207.

26. Wiles, J. A.; Grzybowski, B. A.; Winkleman, A.; Whitesides, G. M. A Tool for Studying Contact Electrification in Systems Comprising Metals and Insulating Polymers. *Anal. Chem.* **2003**, *75*, 4859–4867.

27. Lin, Z.-H.; Zhu, G.; Zhou, Y. S.; Yang, Y.; Bai, P.; Chen, J.; Wang, Z. L. A Self-Powered Triboelectric Nanosensor for Mercury Ion Detection. *Angew. Chem., Int. Ed.* **2013**, *52*, 5065–5069.

28. Lin, Z.-H.; Xie, Y. N.; Yang, Y.; Wang, S. H.; Zhu, G.; Wang, Z. L. Enhanced Triboelectric Nanogenerators and Triboelectric Nanosensor Using Chemically Modified TiO_2 Nanomaterials. *ACS Nano* **2013**, *7*, 4554–4560.

29. Yang, Y.; Zhang, H. L.; Liu, Y.; Lin, Z.-H.; Lee, S. M.; Lin, Z. Y.; Wong, C. P.; Wang, Z. L. Silicon-Based Hybrid Energy Cell for Self-Powered Electrodegradation and Personal Electronics. *ACS Nano* **2013**, *7*, 2808–2813.

30. Stöber, W.; Fink, A.; Bohn, E. Controlled Growth of Monodisperse Silica Spheres in Micron Size Range. *J. Colloid Interface Sci.* **1968**, *26*, 62–69.

31. Westcott, S. L.; Oldenburg, S. J.; Lee, T. R.; Halas, N. J. Formation and Adsorption of Clusters of Gold Nanoparticles onto Functionalized Silica Nanoparticle Surfaces. *Langmuir* **1998**, *14*, 5396–5401.

32. Gu, L.; Cui, N. Y.; Cheng, L.; Xu, Q.; Bai, S.; Yuan, M. M.; Wu, W. W.; Liu, J. M.; Zhao, Y.; Ma, F.; *et al*. Flexible Fiber Nanogenerator with 209 V Output Voltage Directly Powers a Light-Emitting Diode. *Nano Lett.* **2013**, *13*, 91–94.

33. Park, K. I.; Lee, M.; Liu, Y.; Moon, S.; Hwang, G. T.; Zhu, G.; Kim, J. E.; Kim, S. O.; Kim, D. K.; Wang, Z. L.; *et al*. Flexible Nanocomposite Generator Made of $BaTiO_3$ Nanoparticles and Graphitic Carbons. *Adv. Mater.* **2012**, *24*, 2999–3004.